

AGN Coronal Emission models I. The Predicted Radio Emission

I. Ruginski,^{1*} and Ari Laor¹

¹*Physics Department, Technion – Israel Institute of Technology, Haifa 32000, Israel*

ABSTRACT

Accretion discs in AGN may be associated with coronal gas, as suggested by their X-ray emission. Stellar coronal emission includes radio emission, and AGN corona may also be a significant source for radio emission in radio quiet (RQ) AGN. We calculate the coronal properties required to produce the observed radio emission in RQ AGN, either from synchrotron emission of power-law (PL) electrons, or from cyclo-synchrotron emission of hot mildly-relativistic thermal electrons. We find that a flat spectrum, as observed in about half of RQ AGN, can be produced by corona with a disc or a spherical configuration, which extends from the innermost regions out to a pc scale. A spectral break to an optically thin power-law emission is expected around 300-1000 GHz, as the innermost corona becomes optically thin. In case of thermal electrons, a sharp spectral cutoff is expected above the break. The position of the break can be measured with VLBI observations, which exclude the cold dust emission, and it can be used to probe the properties of the innermost corona. Assuming equipartition of the coronal thermal energy density, the PL electrons energy density, and the magnetic field, we find that the energy density in a disc corona should scale as $\sim R^{-1.3}$, to get a flat spectrum. In the spherical case the energy density scales as $\sim R^{-2}$, and is $\sim 4 \times 10^{-4}$ of the AGN radiation energy density. In paper II we derive additional constraints on the coronal parameters from the Gudel-Benz relation, $L_{\text{radio}}/L_{\text{X-ray}} \sim 10^{-5}$, which RQ AGN follow.

Key words: galaxies: active – quasars: absorption lines – quasars: general.

1 INTRODUCTION

What is the origin of the radio emission in Radio Quiet (RQ) AGN? In Radio Loud (RL) AGN the radio emission is often spatially resolved with a jet like structure, which on milli-arcsec (hereafter mas) scales often shows super luminal motion indicative of bulk relativistic motion. In radio quiet AGN (Kellermann et al. 1989; Miller et al. 1993), a significant fraction of the radio emission is often unresolved (Kellermann et al. 1994; Kukula et al. 1998; Leipski et al. 2006; Zuther et al. 2012), even on pc scale (Blundell & Beasley 1998; Caccianiga et al. 2001; Ulvestad et al. 2005a; Doi et al. 2013; Panessa & Giroletti 2013). The observed spectral slopes are often flat, or even inverted (Barvainis et al. 1996; Kukula et al. 1998; Barvainis et al. 2005; Ulvestad et al. 2005a; Behar et al. 2015), which indicates the emission is not just optically thin synchrotron emission, but rather includes some contribution from a compact optically thick source, which can produce a flat or inverted spectrum.

Some of the radio emission in RQ AGN may be produced by starburst activity in the host galaxy (Padovani et al. 2011; Condon et al. 2013), however the bulk of the radio emission likely originates in the AGN activity (White et al. 2015; Zakamska et al. 2016). The radio emission may be spatially extended if it originates in an AGN driven wind which shocks the host galaxy gas (Gallimore et al. 2006; Jiang et al. 2010; Ishibashi & Courvoisier 2011; Zakamska & Greene 2014; Nims et al. 2015). The radio may also originate from a scaled down compact jet emission, where the typical jet power is 10^3 smaller than in RL AGN (Falcke et al. 1995; Wilson & Colbert 1995). Observations of nearby RQ Seyfert galaxies resolve the emission (Giroletti & Panessa 2009; Doi et al. 2013), and show sub relativistic motion on pc scale (Middelberg et al. 2004; Ulvestad et al. 2005b). Indications for a compact pc scale source size are also given by variability (Wrobel 2000; Anderson & Ulvestad 2005; Barvainis et al. 2005; Mundell et al. 2009).

Laor & Behar (2008, hereafter LB08), noted that RQ AGN follow the Gudel-Benz relation, where $L_{\text{R}}/L_{\text{X}} = 10^{-5}$, which coronally active stars follow. Since the X-ray emis-

* E-mail: ruginski.igor@gmail.com

sion in RQ AGN may originate in a corona above the accretion disc, it is natural to assume that the radio emission in RQ AGN may also originate in the corona, as it does in coronally active stars. Although the physical mechanism which leads to the Gudel-Benz relation is not understood yet, and the luminosities associated with AGN and coronally active stars deviate by about 13 orders of magnitude (10^{31} vs. 10^{44} erg s $^{-1}$), the local coronal conditions may be similar (effective temperature, large rotational shear, local densities, see discussion in Gudel 2002). So, it is plausible to expect that similar mechanisms operate in both systems. The maximal possible synchrotron surface emissivity (i.e. brightness temperature) implies that the minimal size of the GHz emission region is on parsec scales (e.g. LB08, eq.22 there), as also suggested by the observed variability (Barvainis et. al 2005). Relativistic electrons may reach this radius through the equivalent of Coronal Mass Ejections (CME) observed in coronally active stars, i.e. magnetized plasma ejected from the innermost accretion disc. Alternatively, the electrons may reside in a corona which forms a thin layer above an accretion disc, which extends out to pc scale. Although the disc on pc scale must be cold, it may still have a surface corona, as also seen in cool M stars which are sometimes coronally active (Gudel 2002).

Synchrotron emission on pc scale, or smaller, may also be produced by a scaled down, low power, jet emission. The difference between a CME and jetted emission is more on the descriptive level, where CME is likely to be poorly collimated and form a sub relativistic outflow, while the term jet is used for a collimated relativistic outflow. Some relativistic jet models in RL AGN invoke a disc corona as the base of the jet (Merloni & Fabian 2002), and in RQ AGN the subsequent acceleration may be missing.

Interestingly, high resolution pc scale imaging of NGC 1068 reveal radio emission aligned with the central obscuring torus (Gallimore et al. 1997, 2004), which provides support for the coronal disc emission scenario for the pc scale radio emission. However, such a pc scale radio emitting corona is clearly not the dominant source of the X-ray emission in unobscured AGN, given the observed X-ray variability on time scales of days or shorter. The observed X-ray emission must come from the innermost accreting region, possibly from an X-ray emitting corona above the innermost disc at a few gravitational radii. Given the maximal intensity of synchrotron emission, the radio emitting corona should be ~ 100 times larger than the X-ray emitting corona. However, since the minimal size of the synchrotron emission region scales as ν^{-1} (LB08), the radio emission at a few hundred GHz can come directly from the X-ray corona (Inoue & Doi 2014).

VLBI observations (Blundell & Beasley 1998; Caccianiga et al. 2001; Ulvestad et. al 2005a) yield lower limits on the brightness temperature of $T_B > 10^8 - 10^9$ K. Although the synchrotron emission is commonly assumed to originate in relativistic electrons with a power-law energy distribution, this limit on T_B is also consistent with synchrotron emission of thermal electrons in the radio corona, for a corona temperature of $T \sim 5 \times 10^9$ K, as measured for the X-ray corona (Fabian et al. 2015).

The purpose of this paper is to calculate the possible range of the radio emission signatures of coronal synchrotron models. These predictions can be used to explore the valid-

ity of the coronal emission scenario, and to possibly probe the physical parameters of the corona. In section 2 we describe the theoretical background, in section 3 the numerical solution scheme, in section 4 we provide useful analytic solution, and in section 5 we present the numerical solution. The discussion is given in section 6, and the conclusions are summarized in section 7. In paper II (Raginski & Laor, in preparation) we calculate the implied X-ray emission of the coronal models used here, and discuss the additional constraints provided by the X-ray observations.

2 THE THEORETICAL BACKGROUND

Electrons accelerate and radiate radio emission either when they pass near charged particle, or when they propagate in a magnetic field. In the earlier case, the free-free spectral slope $\eta = \text{dlog}F_\nu/\text{dlog}\nu$ is ~ -0.1 from the radio to $h\nu \sim kT$. The thermal free-free emission is not viable in objects with a power-law emission with a steeper or a flatter η . Free-free emission of $T > 10^7$ K gas is also excluded as it over predicts the observed X-ray luminosity (e.g. LB08, section 3.6.1 there). Free-free is a viable mechanism if the gas is cooler than 10^7 K, but this is generally ruled out by the VLBI limits of $T_B > 10^8 - 10^9$ K on the core emission. Thus, electrons in a magnetic field is the only generally viable mechanism. Below we briefly review the emission of relativistic electrons with a power-law (PL) energy distribution (synchrotron emission), thermal electrons (cyclotron emission), or mildly relativistic thermal electrons (cyclo-synchrotron emission, hereafter thermal synchrotron emission). We provide expressions for the emission, absorption, and radiation transfer used to derive the observed emission.

2.1 The synchrotron emission and absorption for thermal and PL electrons

An electron in a magnetic field B gyrates around the field lines at a frequency

$$\omega_0 = \frac{eB}{\gamma m_e c} \equiv \frac{\omega_B}{\gamma}, \quad (1)$$

where e is the electron charge, m_e is the mass of the electron, $\gamma = \frac{1}{\sqrt{1-\beta^2}}$ is the Lorentz factor, and $\beta = \frac{v}{c}$, where v is the velocity of the electron. Non relativistic electrons ($\beta \ll 1$) radiate cyclotron emission at ω_B . For mildly relativistic electrons ($\gamma \approx 1$), additional harmonics appear and the emitted spectrum becomes polychromatic with a few additional lines at higher harmonics. As the electrons become more relativistic ($\gamma \gg 1$), higher harmonics appear. The width of each line becomes wider with increasing harmonic number, and finally for high enough value of γ and harmonic number s , adjacent harmonics merge and a continuous spectrum is generated.

The resonant frequencies occur at (Zheleznyakov 1970).

$$\omega_s = \frac{s\omega_0}{(1 - \beta_{||} \cos \alpha)}, \quad (2)$$

where $\beta_{||}$ is the projection of β on the direction of the magnetic field, and α is the angle between the magnetic field and the observer. The pitch angle θ_p is the angle between

the direction of motion of the electron and the magnetic field, which gives

$$\begin{aligned}\beta_{\parallel} &= \beta \cos(\theta_p) \\ \beta_{\perp} &= \beta \sin(\theta_p).\end{aligned}\quad (3)$$

Equation 2 is correct when the refraction index of the medium is unity, which is a good approximation for AGN coronae, as the frequencies of interest are well above the gyration and Langmuir frequencies ($\sim 300\text{MHz}$ for typical condition assumed). We have verified this numerically by solving for the emission spectrum including the corona refractive index.

We used Zheleznyakov (1970, eqs. 26 & 35 there) for the emitted energy per harmonic number per solid angle ($\text{erg sec}^{-1} \text{strd}^{-1}$). The specific emission power ($\text{erg sec}^{-1} \text{strd}^{-1} \text{frequency}^{-1}$) for a unity refraction index is (Mahadevan et. al 1996)

$$\frac{d\epsilon}{dt d\Omega d\omega} = \sum_s \frac{e^2 \omega^2 [\beta_{\perp}^2 J_s'^2(\xi) + (\frac{\cos \alpha - \beta_{\parallel}}{\sin \alpha})^2 J_s^2(\xi)]}{2\pi c} \times \delta[s\omega_0 - \omega(1 - \beta_{\parallel} \cos \alpha)], \quad (4)$$

where ω is the continuum angular frequency, J_s is a Bessel function of order s , J_s' is the first derivative of the Bessel function of order s , and ξ is

$$\xi = \frac{\omega \beta_{\perp} \sin \alpha}{\omega_0}. \quad (5)$$

Equation 4 provides the emission spectrum of a single electron, with kinetic energy of $(\gamma - 1)mc^2$, propagating at a pitch angle of θ_p to the magnetic field. In order to get an expression for the emission per unit frequency per unit volume, i.e. the emission coefficient $P(\omega)$, we need to multiply eq.4 by $n_{\gamma\theta_p}$, the number of electrons with velocities in the range of $[\gamma, \gamma + d\gamma]$ and a pitch angle in the range of $[\theta_p, \theta_p + d\theta_p]$, and integrate over γ . We then integrate over θ_p , and α , by assuming a uniform distribution in both angles, i.e. a random distribution of both the electron velocities and the magnetic field line directions in a given volume,

$$P(\omega) = \int_{\alpha} \int_{\gamma} \int_{\theta_p} p_{\text{single}}(\gamma, \omega, \theta_p) n_{\gamma\theta_p} d\gamma d\theta_p \times 2\pi \sin \alpha d\alpha \quad (6)$$

in units of $\text{erg sec}^{-1} \text{cm}^{-3} \text{Hz}^{-1}$, where $p_{\text{single}}(\gamma, \omega, \theta_p) = \frac{d\epsilon}{dt d\Omega d\omega}$ is the emission of a single electron. In the next sections we will use

$$p_{\text{single}}(\gamma, \nu, \theta_p) = 2\pi p_{\text{single}}(\gamma, \omega, \theta_p) \quad (7)$$

and

$$P(\nu) = 2\pi P(\omega). \quad (8)$$

An expression for the absorption coefficient is given by Rybicki & Lightman (2004, hereafter RL04, eq. 6.50 there). We modify the equation to include the dependence on pitch angle θ_p , which gives

$$\alpha_{\nu} = - \int d\theta_p \frac{c^2}{8\pi\nu^2} \int dE \times p_{\text{single}}(\gamma, \nu, \theta_p) E^2 \frac{\partial}{\partial E} \left(\frac{n(E, \theta_p)}{E^2} \right), \quad (9)$$

where E is the kinetic energy of the electron, and $n(E, \theta_p)$ is the density of electrons per unit energy per pitch angle.

To calculate the radiative transfer we divide the medium into m unit volumes (see below the assumed geometry) of uniform emission and absorption coefficients, say $P_m(\nu)$ and $\alpha_{\nu m}$. If a ray with an intensity I_{m-1} enters this unit volume, and travels a distance of d_m within this volume, then the intensity of the exiting ray is

$$I_m(\nu) = I_{m-1}(\nu) e^{-\alpha_{\nu m} d_m} + \frac{P_m(\nu)}{4\pi\alpha_{\nu m}} \left(1 - e^{-\alpha_{\nu m} d_m} \right) \quad (10)$$

where the first term represents the absorption of the incident intensity, and the second one is the contribution of the emission inside the volume.

2.2 The geometry

2.2.1 Disc Configuration

We assume an optically thick accretion disc which extends from the innermost stable orbit R_{in} at

$$R_0 \equiv 3R_S, \quad (11)$$

where R_S is the Schwarzschild radius,

$$R_S = \frac{2GM_{\text{BH}}}{c^2}, \quad (12)$$

(Shakura & Sunyaev, 1973). We use $M_{\text{BH}} = 10^8 M_{\odot}$ for the black hole (BH) mass. For the outer boundary of the disc we use $R_{\text{out}} = 3 \text{ pc}$, which corresponds to $3 \times 10^5 R_S$. The observed UV spectral energy distribution suggests a maximal temperature $\sim 5 \times 10^4 \text{K}$ (Laor & Davis, 2014), which commonly implies a thin disc with an inner radius $R_{\text{in}} > R_0$. Therefore, in section 5.3 we study the effect of a larger R_{in} on the radio emission spectrum. We assume a blanket - like corona that covers the accretion disc, with a uniform thickness of $H = 10R_S$.

The thermal electrons density is assumed to scale with radius as

$$N(R) = N_0 \times \left(\frac{R}{R_0} \right)^{-q}. \quad (13)$$

We generally assume $N_0 = 10^9 \text{cm}^{-3}$, in order to obtain an optical depth for electron scattering of $\tau_{es} \approx 0.1 - 0.5$ at $R \approx R_0$, as suggested by the X-ray emission (see paper II). In section 5.3 we explore the dependence of the radio spectrum on the value of q .

In addition to the thermal electrons, we assume that the corona also has non thermal electrons with a PL energy distribution. The PL distribution may be generated during reconnection events, which may also set the temperature of the thermal component. The energy distribution of the PL and thermal populations are

$$n_{\text{pl}}(\gamma) d\gamma = C_{\gamma} \gamma^{-\delta} d\gamma \quad (14)$$

$$n_{\text{th}}(\gamma) d\gamma = \frac{N\gamma^2\beta}{\Theta K_2(\Theta)} e^{-\frac{\gamma}{\Theta}},$$

where C_{γ} is a normalization constant, δ is the power index of the PL distribution (typically $\delta = 2$ or 3 , see section 5.4), and Θ is the normalized temperature $\Theta \equiv \frac{kT}{mc^2}$, and K_2 is the modified Bessel function of the second kind. The expression for $n_{\text{th}}(\gamma)$ is the Maxwell - Juttner distribution, which is the relativistic form of Maxwell Boltzmann.

The energy density of the two populations is assumed to be in equipartition, i.e.

$$\int_{\gamma_{\min}}^{\gamma_{\max}} C_{\gamma}(\gamma - 1)mc^2\gamma^{-\delta}d\gamma = \frac{3}{2}NkT, \quad (15)$$

which is used to derive the value of C_{γ} .

The electron temperature in the corona is generally assumed to be $T = 5 \times 10^9 K$, at all radii. This temperature is naturally expected for a two temperature corona (Di Matteo et al. 1997), for a corona heated by magnetic reconnection (Di Matteo, 1998), and also for a pair plasma corona (Svensson 1984; Lightman & Zdziarski 1987; Haardt & Maraschi 1991, 1993). In addition, recent *NuSTAR* hard X-ray spectroscopy of AGN (Fabian et al. 2015) indeed provide direct evidence for a corona with $kT \sim 0.1m_e c^2$, i.e. $T \sim 5 \times 10^9 K$. However, we also explore below the effect of using a lower T .

We assume that the local value of the magnetic field within the corona is in equipartition with the thermal electrons, i.e.

$$\frac{B^2(R)}{8\pi} = \frac{3}{2}N(R)kT. \quad (16)$$

In the numerical calculations we also explore deviations from equipartition, in addition to exploring the effects of different values for N_0 , q , δ , and R_0 .

2.2.2 Spherical Configuration

For this configuration, we assume a spherical symmetry around the BH. The corona extends for a range of radii $R_0 < R < R_{\text{out}}$. The temperature is fixed at $T = 5 \times 10^9 K$, and N is given by eq.13. The synchrotron emission of both thermal and PL distributions are calculated as described in section 3.

3 THE NUMERICAL SOLUTION SCHEME

For the thermally distributed electrons, $n_{\text{th}}(\gamma)d\gamma$ is set up using eq.14 for $1.01 < \gamma < 10$, using 180 bins uniformly spaced logarithmically. For the PL electrons, $n_{\text{pl}}(\gamma)d\gamma$ is derived for $1.1 < \gamma < 3000$ with 300 bins uniformly spaced logarithmically. The upper value of γ is selected to ensure that the peak emission of individual electrons, $\nu = 4.1\gamma^2 B$ MHz (RL04, eq.6.17c there), extends to $\nu > 100$ GHz for the values of B used here. The pitch angle θ_p is spanned linearly in 14 bins between 0 and π .

The number of electrons per unit pitch angle per unit energy are

$$n_{\text{th}}(\gamma, \theta_p)d\gamma d\theta_p = n_{\text{th}}(\gamma)d\gamma \sin \theta_p d\theta_p / 2, \quad (17)$$

and

$$n_{\text{pl}}(\gamma, \theta_p)d\gamma d\theta_p = n_{\text{pl}}(\gamma)d\gamma \sin \theta_p d\theta_p / 2. \quad (18)$$

3.1 The emission and absorption coefficients

The analytical expression for the spectrum emitted by a single electron (eq.4) includes a delta function. We

use the following approximation for the delta function (Mahadevan et. al 1996)

$$\delta[s\omega_0 - \omega(1 - \beta_{\parallel} \cos \alpha)] = \frac{f(\chi)}{\omega_B(1 - \beta_{\parallel} \cos \alpha)}, \quad (19)$$

where ω_B is the Larmour frequency (eq.1), and $f(\chi)$ is

$$f(\chi) = \frac{15}{16\Delta\chi} \left[1 - \left(\frac{2}{\Delta\chi^2} \right) (\chi - \chi_s)^2 + \left(\frac{1}{\Delta\chi^4} \right) (\chi - \chi_s)^4 \right], \quad (20)$$

where χ and χ_s are

$$\chi = \frac{\omega}{\omega_B}, \quad \chi_s = \frac{\omega_s}{\omega_B}. \quad (21)$$

For the harmonic line width we use $\Delta\chi = 0.05\chi_s$ (Mahadevan et. al 1996). Combining eq.19 and eq.4 we get the emission per single electron

$$p_{\text{single}}(\gamma, \omega, \theta_p) = \sum_s \frac{e^2 \omega^2 [\beta_{\perp}^2 J_s'^2(\xi) + \left(\frac{\cos \alpha - \beta_{\parallel}}{\sin \alpha} \right)^2 J_s^2(\xi)]}{2\pi c \omega_B (1 - \beta_{\parallel} \cos \alpha)} \times f\left(\frac{\omega}{\omega_B}\right). \quad (22)$$

In order to calculate the emission coefficient per frequency, we need to numerically integrate over the relevant electron energy distribution, pitch angle, and observer angle α (eq.6). The absorption coefficient is calculated using eq.9.

Figure 1 compares the numerical solutions for the emission and absorption coefficients described above, with the analytical expression given by RL04 (eq.6.36 there) for the PL energy distribution. The analytical and the numerical solutions fit well for $\nu > 10^9$ GHz, the region where the emission and absorption are produced by $\gamma \gg 1$ electrons, where the analytical approximation is valid. The numerical solution deviates from the analytic one at low ν since the analytic calculation applies only at $\gamma \gg 1$. We verified the validity of our calculation for the thermal distribution by comparing our results with the results of Wardzinski & Zdziarski (2000, figure 5 there), which our results overlap.

3.2 The integrated Radio emission from a disc corona

Given the emission and absorption coefficients presented above, we now calculate the total emission of the disc corona. Figure 2 presents the geometry assumed in order to integrate the emission along various lines of sight. We start with a ray emitted at a given angle θ_e and azimuth angle ϕ_a , from a given position on the upper surface of the disc corona. The contribution to the intensity is integrated along the ray inside the corona until it reaches the face of the underlying optically thick accretion disc, or the side-walls of the coronal disc (see Fig.2). The integration stops inwards of the innermost part of the disc, $R < R_0$, which represents light trapping by the BH. The path of the ray is divided into segments, where every segment is a track of the ray inside a specific coronal ring. We use eq.10 to calculate the change in intensity following the passage of each segment. The radii of the coronal rings are logarithmically distributed between R_0 and R_{out} , according to the values presented in section 2.2. In case of emission from PL electrons, the corona is divided into 25 rings, where the outermost rings is at $R_{\text{out}} = 3 \times 10^5 R_S$. For thermal electrons,

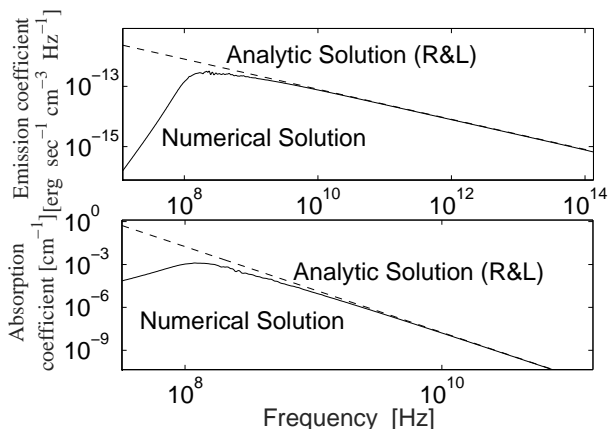


Figure 1. A comparison between numerical and analytical results for the emission and absorption coefficients for PL electrons. The model assumes B which is in equipartition with a thermal component, where $N = 10^9 \text{ cm}^{-3}$ and $T = 10^9 \text{ K}$ (eq.16), and a PL electron distribution with $\delta = 2$, which is also in equipartition (eq.15). The numerical results overlap well the analytic results (RL04) at $\nu > 10^9 \text{ GHz}$, the region dominated by the emission of $\gamma \gg 1$ electrons, where the analytic approximation applies.

the corona is extended up to $R_{\text{out}} = 5 \times 10^4 R_S$, and divided into 40 rings.

The intensity of a specific ray then is multiplied by a geometrical factor of $\cos \theta_e$ that stands for the inclination of the emitting area element. The next step is to integrate the emission from a given ring. This integration is equivalent to a sum of all rays emitted azimuthally from the same point of "coronal face", i.e. an integral over the azimuthal angle $\phi_a \in [0, 2\pi]$.

$$F_i(\nu) = \sum_{\phi_a=0}^{2\pi} I_{\text{ray}}(\nu) \cos(\theta_e) \Delta\phi_a, \quad (23)$$

where $F_i(\nu)$ is the flux emitted at a given angle of inclination, from a ring designated by i , and I_{ray} is the intensity of a specific ray emitted from the corona, calculated according to eq.10.

We multiply the flux by $R\Delta R$, to get the ring emission (the factor of 2π is included above in the integration over ϕ). We then integrate on radii $R_0 < R < R_{\text{out}}$ to obtain the total luminosity of the disc.

$$L_\nu = 4\pi \sum_{R_i=R_0}^{R_{\text{out}}} R F_i(\nu) \Delta R_i, \quad (24)$$

where L_ν is the total radio luminosity of the disc corona at inclination angle of θ_e , and the factor of 4π is used to calculate the inferred isotropic emission even in a non-isotropic case.

3.3 The integrated Radio emission from a spherical corona

Figure 3 presents the geometry assumed in the spherical case. The corona is divided into spherical concentric shells, each with a uniform B and N , while the value of T is the same at all shells. The intensity from a given unit area on

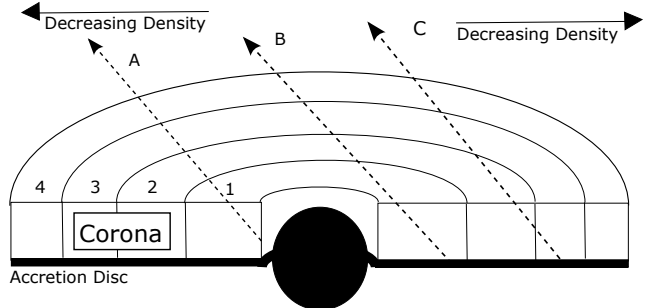


Figure 2. An illustration of the geometry used for the disc corona. The corona is divided into rings, and three rays (A, B and C), are emitted from the surface to the same direction (and thus seen by the same observer). Ray A is emitted from the first ring, and traced back to its origin at the inner wall of the corona. Ray B originates and is emitted from ring 1. Ray C starts in the third ring, and emitted from the second.

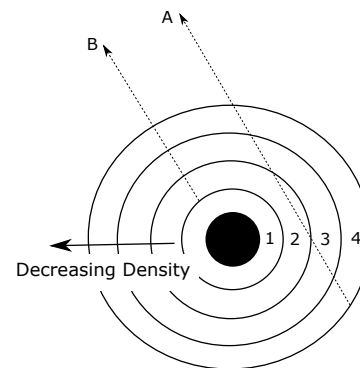


Figure 3. An illustration of the geometry used for the spherical corona, which is divided into spherical shells. Two rays are drawn, all of them are emitted towards the same observer. Ray B originates on the innermost shell, as the radiation path cannot pass the BH.

the face of the outer shell, is calculated by shooting rays back in all directions. Given the azimuthal symmetry of the radiation transfer, we need to sample only $\theta_e \in [0, \pi/2]$. Each ray is linearly traced within the corona, and its intensity is calculated according to eq.10 for all segments along its path, as is done for the case of disc corona. Knowing the intensity per frequency for each ray, we multiply the result by a Jacobian factor of $\sin \theta_e \cos \theta_e$ and by a factor of 2π for integration on azimuthal direction. All the rays are summed, and their intensities are numerically integrated on angles to obtain the flux.

$$F_\nu = \sum_{\theta_e=0}^{\pi/2} 2\pi I_{\text{ray}}(\nu) \cos(\theta_e) \sin \theta_e \Delta\theta_e \quad (25)$$

The derived flux per unit frequency is then multiplied by a factor of $4\pi R_{\text{out}}^2$ to obtain the luminosity.

$$L_\nu = 4\pi R_{\text{out}}^2 F_\nu \quad (26)$$

A major difference between the disc and the sphere is that in the disc case we see directly the emitting surface area at each ring, so the integrated emission is to a good approximation just a simple superposition of the emission of the individual rings. In contrast to the spherical case, the

radiation passes from the emission radius to the emitting surface. So, we see down to the effective photosphere, i.e. the radius where the optical depth reaches unity, at a given frequency. As a result, the contribution to the emission at a given ν comes from a larger range in R in the disc case, compared to the sphere case (see section 5.1).

4 AN APPROXIMATE ANALYTICAL SOLUTION FOR THE RADIO SPECTRAL SLOPE

The spectral slope, $\eta \equiv d \log L_\nu / d \log \nu$, of synchrotron emission from a uniform source of PL electrons, is $\eta = -(\delta - 1)/2$ for optically thin emission, and $\eta = 2.5$ for optically thick emission. For thermal electrons $\eta = 2$ in the optically thick Rayleigh-Jeans regime, with a sharp exponential drop when the emission becomes optically thin. Below we derive approximate analytical solutions for η for a non uniform synchrotron source, following either the disc or the spherical distribution, and for either thermal or PL energy distributions. The derived expressions can be used to link the observed η and the structural parameters of the corona.

The overall spectrum of a stratified corona is a superposition of the spectra of all the rings or shells within the corona. Each ring or shell emits synchrotron radiation with a characteristic spectrum which rises with ν in the optically thick part and drops in the optically thin part. The peak occurs at $\nu_{\text{peak}}(R)$ which corresponds to the optically thick to thin transition. The transition occurs when the optically thick emission curve (blackbody emission in the thermal electrons case), intersects the optically thin emission curve, as derived for the local conditions at a given R . Below we derive a general expression for ν_{peak} as a function of the properties of the emitting region, for thermal and PL electrons. We then use it to derive $\nu_{\text{peak}}(R)$ for the specific corona models we use.

To estimate η , we assume the emission at a given ν is dominated by the emission from the ring/shell where $\nu = \nu_{\text{peak}}$. The implied η is then derived by taking the ratio of the relative increase in $L_{\nu_{\text{peak}}}(R)$, the integrated emission from R_{min} to R , to the ratio of the relative increases in ν_{peak} , by the emission from a given ring/shell of a width ΔR at a distance R , i.e.

$$\eta = \frac{\Delta \log(L_\nu)}{\Delta \log(\nu)} = \frac{\frac{d \log(L_{\nu_{\text{peak}}}(R))}{dR} \Delta R}{\frac{d \log(\nu_{\text{peak}}(R))}{dR} \Delta R} \quad (27)$$

Below, we derive analytic expressions for $\nu_{\text{peak}}(R)$ and $L_{\nu_{\text{peak}}}(R)$ for the PL and thermal electron distributions for the disc and the sphere configurations, and substitute them into the expression above to derive an analytic expression for η .

4.1 Analytic derivation of ν_{peak} for a slab of PL electrons

In this section we assume a slab of thickness H , which consists of PL electrons with an energy density set by equipartition with thermal electrons $E = \frac{3}{2} N k T$. The absorption

coefficients is (RL04)

$$\alpha_\nu = \frac{\sqrt{3} q^3}{8 \pi m} \left(\frac{3q}{2 \pi m^3 c^5} \right)^{\delta/2} C_E (B \sin \theta_p)^{\frac{\delta}{2} + 1} \Gamma \left(\frac{3\delta + 2}{12} \right) \times \Gamma \left(\frac{3\delta + 22}{12} \right) \nu^{-\left(\frac{\delta+4}{2}\right)} \quad (28)$$

The equipartition magnetic field B , and the particle normalization C_E , are

$$B = \sqrt{12 \pi N k T} \quad (29)$$

$$C_E = \frac{3 N k T}{2 \int_{E_{\text{min}}}^{E_{\text{max}}} E^{1-\delta} dE} \equiv \frac{3 N k T}{2 K},$$

where K is the integral in the denominator.

The turnover (peak) frequency satisfies

$$\alpha_{\nu_{\text{peak}}} H = \tau \simeq 1, \quad (30)$$

which gives

$$\nu_{\text{peak}} = \left(\frac{16 \pi m K \left(\frac{3q}{2 \pi m^3 c^5} \right)^{-\delta/2} \left(\sqrt{12 \pi k} \sin \theta_p \right)^{-\frac{\delta}{2} - 1}}{3 \sqrt{3} q^3 k \Gamma \left(\frac{3\delta + 2}{12} \right) \Gamma \left(\frac{3\delta + 22}{12} \right)} \right)^{-\frac{2}{\delta+4}} \quad (31)$$

$$= AT^{\frac{\delta+6}{2(\delta+4)}} N^{\frac{\delta+6}{2(\delta+4)}} H^{\frac{2}{\delta+4}},$$

where A is a constant at a given θ_p .

For PL electrons with $\delta = 2$ we get

$$\nu_{\text{peak}} \approx 1.78 \times 10^{-5} T^{2/3} N^{2/3} H^{1/3} \text{ Hz} \quad (32)$$

It is interesting to compare the above expression to an analogous result presented by Gudel (2002, eq. 22 there), for stellar radio emission

$$\nu_{\text{peak-Gudel}} = \left[10^{11.77+3.44\delta} (\delta - 1)^2 n^2 H^2 B^{\delta+2} \right]^{\frac{1}{\delta+4}} \text{ Hz}, \quad (33)$$

where n is the number density of the PL electrons (generally $n \ll N$). Using the above expression, and applying equipartition of the thermal electrons, PL electrons, and the magnetic field, we obtain

$$\nu_{\text{peak-Gudel}} \propto N^{\frac{\delta+6}{2(\delta+4)}} T^{\frac{\delta+6}{2(\delta+4)}} H^{\frac{2}{\delta+4}}. \quad (34)$$

For $\delta = 2$, and applying equipartition, one obtains

$$\nu_{\text{peak-Gudel}} \approx 7 \times 10^{-6} T^{2/3} N^{2/3} H^{1/3} \text{ Hz}, \quad (35)$$

i.e. the same functional dependence derived above. The coefficient in Gudel is a factor of 2.5 too small, which may reflect the accuracy of the approximate analytic derivations.

4.2 Analytic derivation of ν_{peak} for a slab of thermal electrons

There is no simple analytic expression for the synchrotron absorption coefficient α_ν for electrons with a thermal energy distribution. Instead, we use the numerical results to obtain a fitting function for ν_{peak} as a function of T , N and H . The derived fitting function is

$$\nu_{\text{peak}} = 3.74 \times 10^{-9} T^{1.42} N^{0.55} H^{0.09} \text{ Hz} \quad (36)$$

for $T = 10^8 - 10^{10}$ K, $N = 10^8 - 10^{10}$ cm $^{-3}$, and $H = 10^{14} - 10^{15}$ cm.

Gudel (2002) derives a similar expression

$$\nu_{\text{peak-Gudel}} = 1.3 \left(\frac{NH}{B} \right)^{0.1} T^{0.7} B \quad (37)$$

which gives for an equipartition B

$$\nu_{\text{peak-Gudel}} = 4.8 \times 10^{-7} T^{1.15} N^{0.55} H^{0.1} \quad (38)$$

Note the difference between the power indices of T in eq.36 (1.42) and eq.38 (1.15). The calculation in Gudel (2002) is performed only for relatively low harmonic numbers: $10 < s < 100$, which are relevant for the stellar corona, where $T < 10^8$ K. Imposing the same limitations on the harmonic numbers in our simulation, we derive $\nu_{\text{peak}} \propto T^{1.1}$, in reasonable agreement with the power of 1.15 in Gudel (2002). This difference stresses the need to retain high harmonic numbers in the calculations for mildly relativistic thermal electrons.

Additional comparison was performed with the results of an analogous calculation of the peak frequency performed by Wardzinski & Zdziarski (2000, eq.18 there). Applying equipartition to their expression gives $\nu_{\text{peak}} \sim 5.2 \times 10^{-8} T^{1.45} N^{0.5} H^{0.05}$. The small deviation in the power indices from our expression (eq.36) reflects the uncertainty in the fits to the numerical results. The difference between the coefficients is "compensated" by the small difference in the powers of T , leading to similar values of ν_{peak} at the relevant range of temperatures.

4.3 The spectral slope for emission from a disc

Below we calculate η for synchrotron emission from a disc for both thermal and PL electrons. For the sake of simplicity we assume a constant H , and for T and N we assume

$$\begin{aligned} T(R) &= T_0 \left(\frac{R}{R_0} \right)^{-p}, \\ N(R) &= N_0 \left(\frac{R}{R_0} \right)^{-q}. \end{aligned} \quad (39)$$

4.3.1 Thermal Electrons

Substituting the above $N(R)$, $T(R)$, and a constant H , into eq.36 gives

$$\nu_{\text{peak}}(R) \propto R^{-1.42p-0.55q}. \quad (40)$$

The spectrum of a ring of thermally distributed electrons is that of Rayleigh-Jeans emission, i.e. rises as ν^2 in the optically thick range, and is exponentially falling in the optically thin range. The specific luminosity L_ν at frequency ν is

$$L_{\nu_{\text{peak}}}(R) = \int_{R_{\text{min}}}^R \pi \mathcal{B}_{\nu_{\text{peak}}}(r) 2\pi r dr \quad (41)$$

where $\mathcal{B}_{\nu_{\text{peak}}}(r)$ is the value of the blackbody emission at radius r , and at a frequency $\nu_{\text{peak}}(R)$. We integrate only on rings inner to R , because they are optically thick at a frequency of $\nu_{\text{peak}}(R)$ and their contribution is not negligible. The outer rings, at $r > R$, are optically thin at $\nu_{\text{peak}}(R)$, and their contribution is very small due to the fast exponential drop of the optically thin thermal synchrotron spectrum.

Since $h\nu (\sim 10^{-3} \text{eV}) \ll kT (\sim 100 \text{keV})$, the Rayleigh-Jeans approximation applies,

$$\mathcal{B}_{\nu_{\text{peak}}}(r) = \frac{2\nu_{\text{peak}}^2(R)kT(r)}{c^2}. \quad (42)$$

Substituting eqs. 39, 40 and 42 into eq.41, and setting $R_0/R \ll 1$, we obtain

$$L_{\nu_{\text{peak}}}(R) \propto R^{2-3.84p-1.1q}. \quad (43)$$

Substituting eq.43 and eq.40 into eq.27, gives

$$\eta_{\text{disc-thermal}} = \frac{2 - 3.84p - 1.1q}{-1.42p - 0.55q}. \quad (44)$$

4.3.2 PL electrons

As in the thermal case, for PL electrons we substitute eq.39 into eq.31, and get

$$\nu_{\text{peak}}(R) \propto R^{-\frac{\delta+6}{2(\delta+4)}p - \frac{\delta+6}{2(\delta+4)}q}. \quad (45)$$

The luminosity is

$$L_{\nu_{\text{peak}}}(R) = 2\pi \int_{R_0}^R \frac{P_{\nu_{\text{peak}}}(r)}{4\pi\alpha\nu_{\text{peak}}(r)} 2\pi r dr, \quad (46)$$

where the factor of π outside of the integral converts the source function to flux, and the factor of 2 accounts for the two faces of the disc. This expression holds in areas where the corona is optically thick, which holds at $r < R$ for $\nu = \nu_{\text{peak}}(R)$.

According to RL04, $P_{\nu_{\text{peak}}}$ is given by

$$\begin{aligned} P_{\nu_{\text{peak}}} &= \frac{\sqrt{3}q^3 C_\gamma B \sin \theta_p}{mc^2(\delta+1)} \Gamma\left(\frac{\delta}{4} + \frac{19}{12}\right) \Gamma\left(\frac{\delta}{4} - \frac{1}{12}\right) \\ &\quad \times \left(\frac{2\pi mc\nu_{\text{peak}}}{3qB \sin \theta_p} \right)^{-\frac{\delta-1}{2}}. \end{aligned} \quad (47)$$

Applying equipartition (eq.16) and the expression for C_γ (eq.15) gives

$$P_{\nu_{\text{peak}}}(r) \propto n^{\frac{5}{4}+\frac{\delta}{4}} T^{\frac{5}{4}+\frac{\delta}{4}} \nu_{\text{peak}}^{-\frac{\delta-1}{2}}(R), \quad (48)$$

Applying the radial dependence (eq.39) gives

$$P_{\nu_{\text{peak}}}(r) \propto r^{-(\frac{5}{4}+\frac{\delta}{4})p - (\frac{5}{4}+\frac{\delta}{4})q} \nu_{\text{peak}}^{-\frac{\delta-1}{2}}(R). \quad (49)$$

The absorption coefficient (eq.28), with equipartition (eq.16), gives

$$\alpha_{\nu_{\text{peak}}} \propto n^{\frac{\delta}{4}+\frac{3}{2}} T^{\frac{\delta}{4}+\frac{3}{2}} \nu_{\text{peak}}^{-\frac{\delta+4}{2}}(R). \quad (50)$$

Applying the radial dependence (eq.39) gives

$$\alpha_{\nu_{\text{peak}}} \propto r^{-(\frac{\delta}{4}+\frac{3}{2})p - (\frac{\delta}{4}+\frac{3}{2})q} \nu_{\text{peak}}^{-\frac{\delta+4}{2}}(R). \quad (51)$$

The luminosity density is then (eq.46)

$$\begin{aligned} L_{\nu_{\text{peak}}}(R) &= \nu_{\text{peak}}^{5/2}(R) \int_{R_0}^R \frac{r^{-(\frac{5}{4}+\frac{\delta}{4})p - (\frac{5}{4}+\frac{\delta}{4})q}}{r^{-(\frac{\delta}{4}+\frac{3}{2})p - (\frac{\delta}{4}+\frac{3}{2})q}} r dr \\ &= \nu_{\text{peak}}^{5/2}(R) \int_{R_0}^R r^{\frac{2}{4}+\frac{q}{4}+1} dr, \end{aligned} \quad (52)$$

which gives

$$L_{\nu_{\text{peak}}}(R) \propto \nu_{\text{peak}}^{5/2}(R) R^{-\frac{2}{4}-\frac{q}{4}+2}. \quad (53)$$

for $R \gg R_0$.

Applying the expression for $\nu_{\text{peak}}(R)$ (eq.45) gives

$$L_{\nu_{\text{peak}}}(R) \propto \left(R^{-\frac{\delta+6}{2(\delta+4)}p - \frac{\delta+6}{2(\delta+4)}q} \right)^{5/2} R^{\frac{p}{4} + \frac{q}{4} + 2} = R^{-\frac{5(\delta+6)}{4(\delta+4)}p + \frac{p}{4} - \frac{5(\delta+6)}{4(\delta+4)}q + \frac{q}{4} + 2}, \quad (54)$$

or

$$L_{\nu_{\text{peak}}}(R) \propto R^{-\frac{17}{12}(p+q)+2}, \quad (55)$$

for the $\delta = 2$ case. The derived spectral slope (eq.27) is

$$\eta_{\text{disc-pl}} = \frac{17(p+q) - 24}{8(p+q)}, \quad (56)$$

while for the $\delta = 3$ case we get

$$\eta_{\text{disc-pl}-\delta-3} = \frac{19(q+p) - 28}{9(q+p)}. \quad (57)$$

Note that the above analytic estimate for η for PL electrons is valid only at $\eta > -\frac{\delta-1}{2}$, since this estimate ignores the contribution of the optically thin region, which sets this lower limit on η .

4.4 The spectral slope for emission from a sphere

The emission from a sphere is qualitatively different from disc emission. In the case of a disc, the emission can be considered as a superposition of rings, each one is directly observed. The emission from a sphere can be considered as a superposition of spherical shells, but the emission of each shell propagates through all outer shells, and we effectively see only the emission from a volume set by the surface and the $\tau \approx 1$ radius, deeper shells do not contribute. The thickness of each shell is set by the scale length of $B(R)$, i.e. (Gudel 2002)

$$H(R) = \frac{B(R)}{|\nabla B(R)|} \sqrt{\frac{kT}{mc^2}}. \quad (58)$$

Using the equipartition for $B(R)$, $N(R)$ and $T(R)$ (eqs. 15,16), gives $B \propto R^{-\frac{p+q}{2}}$ and $\nabla B \propto R^{-\frac{p+q}{2}-1}$, which gives

$$H(R) \propto R^{1-\frac{p}{2}}, \quad (59)$$

which we use below to estimate the spectral slope.

4.4.1 Thermal electrons

Applying the expression for $\nu_{\text{peak}}(N, T, H)$ (eq.36) for the sphere yields

$$\nu_{\text{peak}}(R) \propto R^{0.09-1.465p-0.55q}. \quad (60)$$

To derive L_ν we assume the emission originates only from the shell at R , which produces a peak at ν , which gives

$$L_{\nu_{\text{peak}}}(R) = 4\pi R^2 \pi \mathcal{B}_\nu, \quad (61)$$

where \mathcal{B}_ν is the Planck function of a shell R . Thus

$$L_{\nu_{\text{peak}}}(R) \approx \frac{8\pi^2 h \nu_{\text{peak}}^2(R) kT(R)}{c^2} R^2 \propto R^{2.18-3.93p-1.1q}, \quad (62)$$

which gives

$$\eta_{\text{sphere-thermal}} = \frac{2.18 - 3.93p - 1.1q}{0.09 - 1.465p - 0.55q} \quad (63)$$

4.4.2 PL electrons

In this case we apply (eq.31) for ν_{peak} , which gives using eq.39 and eq.59

$$\nu_{\text{peak}}(R) \propto R^{-\frac{4-p\delta-q\delta-8p-6q}{2(\delta+4)}}. \quad (64)$$

The luminosity is given by

$$L_{\nu_{\text{peak}}}(R) = \frac{P_{\nu_{\text{peak}}}(R)}{\alpha_{\nu_{\text{peak}}}(R)} \pi R^2 dR,$$

where $P_{\nu_{\text{peak}}}$ is the emission coefficient (eq.49) and $\alpha_{\nu_{\text{peak}}}$ is the absorption coefficient (eq.51), which yields

$$L_{\nu_{\text{peak}}}(R) \propto R^{-\frac{-2p\delta-2q\delta-18p-13q+26+4\delta}{2(\delta+4)}}. \quad (65)$$

The implied slope for $\delta = 2$ is

$$\eta_{\text{sphere-pl}} = \frac{22p + 17q - 34}{10p + 8q - 4}. \quad (66)$$

As noted above, the expressions for $\eta_{\text{sphere-thermal}}$ and $\eta_{\text{sphere-pl}}$ are valid only for slopes above the optically thin range, i.e. for $\eta > -(\delta - 1)/2$.

5 RESULTS

Below we present the results of the numerical calculations of the radio emission. The calculations are for the disc and spherical geometries, and for thermal and PL electrons. In all cases we assume an isothermal corona, and a decreasing $N(R)$, i.e. $p = 0$, and $q > 1$ (eq.39). The value of $B(R)$ is derived from the assumption of equipartition with the thermal electrons (eq.16). The PL electrons are also assumed to be in equipartition with the thermal electrons (eq.15).

The innermost radius of the corona is assumed to be the last stable orbit for a central BH of a mass of $10^8 M_\odot$ (eqs.11, 12), unless noted otherwise. The outermost radius is taken to be $5 \times 10^4 R_S$ for the thermal distribution, and $3 \times 10^5 R_S$ for the PL electrons, which ensures the spectral break due to transition to optically thick emission occurs at $\nu < 1$ GHz (see below). As noted above, the coronal thickness in the disc configuration is assumed to be constant at $H = 10R_S$.

We concentrate below on models which yield a flat spectral slope, as this is the unique signature of a compact emission source, such as a disc corona. As shown below, for some parameters the optically thin emission from the outer parts of the corona, can dominate the emission from the inner parts. In such a case, the overall spectrum is just that of an optically thin source, which is derived also in other more extended emission models.

5.1 The radial dependence of the emission

Figures 4 and 5 present typical spectra of thermal and PL distributed electrons within a disc or spherical corona. The values of the density distribution q parameters were selected to produce a flat spectrum ($L_\nu \propto \nu^0$) in the intermediate frequency range (1-100 GHz), before reaching the steeply falling optically thin limit at higher frequencies, and the steeply rising optically thick emission at lower frequencies. The figures also present the contributions to the total emission of different rings or spherical shells.

The emission of thermal electrons from a given ring or

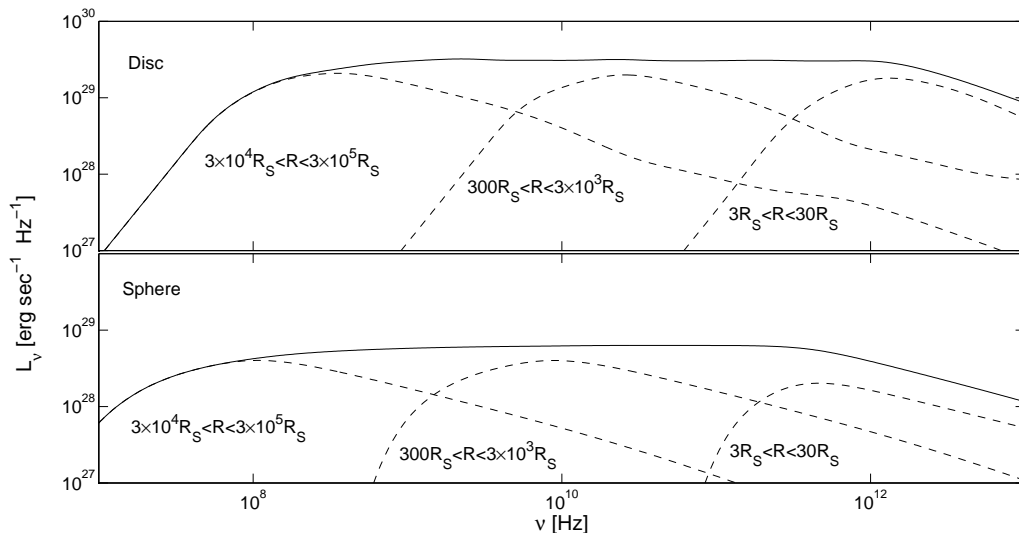


Figure 4. The spectrum of PL electrons ($\delta = 2$) from a corona in a disc (upper panel) or a sphere (lower panel). The disc is observed at an inclination angle of $\cos \theta_e = 0.5$. The solid line in each panel represents the overall emission, and the dashed lines the contributions of different rings or shells. The corona is isothermal with $T = 10^9 \text{ K}$. The coronal density drops as a PL with $q = 1.4$ for a disc, and $q = 2$ for a sphere, selected to produce a flat continuum, and $N_0 = 10^9 \text{ cm}^{-3}$ to set the luminosity scale (see section 5). The emission below 1 GHz originates mostly at $R > 3 \times 10^4 R_S$, i.e. $R > 10^{18} \text{ cm}$ for $M_{\text{BH}} = 10^8 M_\odot$ used here. At 100 GHz (3 mm) the emission comes mostly from $R \sim 100 R_S$. The emission at $\nu > 10^{12} \text{ Hz}$ in RQ AGN is heavily dominated by cold dust emission, but may be measured with VLBI which detects only high T_b sources.

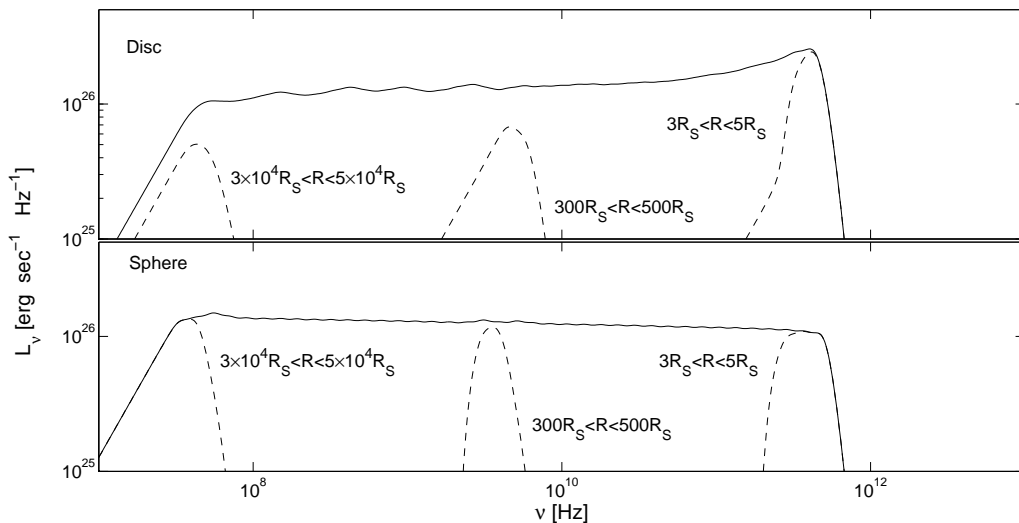


Figure 5. The synchrotron emission of the thermal electrons at $T = 5 \times 10^9 \text{ K}$, for the same configurations as in Fig.4. The coronal density drops with $q = 1.82$ for a disc, and $q = 1.98$ for a sphere, with $N_0 = 10^9 \text{ cm}^{-3}$ (see section 5 for further details). Although the thermal electrons are in equipartition with the PL electrons, their synchrotron luminosity is significantly smaller than that produced by the PL electrons. Note also the narrow range of frequencies of the emission from a given ring or shell, in contrast with the broad distribution of the PL electrons emission. The wiggles appearing in the spectrum are a numerical artefact caused by the finite resolution of the radial integration.

shell (Fig.5), covers a smaller range of frequencies, compared to the emission of the PL electrons (Fig.4). Both electron distributions produce similar spectral slopes in the locally optically thick emission at $\nu < 100\text{MHz}$ (2 for thermal, 2.5 for PL in a disc), but in the locally optically thin part the thermal emission shows a sharp exponential drop, while the PL show only the gradual optically thin falloff with a slope of $-1/2$. The sharp cutoff of the optically thin thermal synchrotron results from the exponential drop in the electron energy (eq.14), together with the exponential drop in the emission of a single electron (eq.6.34b in RL04).

The slope of the locally optically thick emission in the spherical configuration is steeper than in the disc configuration, as the emission is absorbed by the outer shells. In contrast with the disc case, where the emission from each ring is directly observed.

5.2 The inclination dependence of the emission

Figure 6 presents the observed disc emission for PL and thermal electrons as a function of $\cos\theta_e$, where θ_e the disc inclination angle. The spectrum can be roughly divided into three regimes, with different inclination dependence. At low enough frequencies, the whole disc is optically thick, and the luminosity scales as $\cos\theta_e$. At high enough frequencies the whole disc is optically thin, the emission becomes isotropic, and the spectra from all inclinations overlap.

At intermediate frequencies, the inner part of the disc is optically thick and an outer part of it is optically thin. The transition radius decreases with increasing frequency, until the whole disc emission becomes optically thin. As a result, at intermediate frequencies we get an intermediate inclination dependence. In the thermal case, the exponential drop in the locally optically thin emission, leads to a negligible contribution from the optically thin isotropically emitting part of the disc. As a result, the optically thick inclination dependence remains $\cos\theta_e$ to almost the highest frequencies.

A peculiar behavior occurs for the thermal case at $\nu > 10^{11}\text{Hz}$ at high inclination (lower panel of Fig.6), where the luminosity at $\cos\theta_e = 0.1$ becomes comparable, and even exceeds the emission at $\cos\theta_e = 0.9$ (for $\nu \approx 5 \times 10^{11}\text{Hz}$). This results from the adopted geometry, as the highest frequency thermal emission comes mostly from the innermost ring, where the height $H = 10R_S$ becomes larger than the radius. Most of the emitting area is now in the walls, and the emission becomes stronger at high inclinations, where the projected area of the walls becomes largest. Thermal synchrotron emission therefore provides a sensitive measure of the projected surface area of the region where the observed frequency is produced.

5.3 The dependence of the emission on the coronal properties

Figure 7 presents the emission of PL electrons from a disc (left panels) or a sphere (right panels). In all cases we assume a PL index $\delta = 2$, and corona with $T = 10^9\text{K}$ with a constant thickness, which extends from $R_{\text{in}} = 3R_S$ to $R_{\text{max}} = 3 \times 10^5 R_S$ for $M_{\text{BH}} = 10^8 M_{\odot}$ (which corresponds to $R_S = 3 \times 10^{13}\text{cm}$). The upper panels present the dependence of the spectrum on the coronal thermal energy density

NkT , where we assume an equipartition with the PL electrons energy density, and the magnetic energy density. As NkT increases, i.e. the normalization of N increases, the luminosity increases, as does the transition frequency from optically thick emission (the 2.5 slope) to a flat continuum. Note also that the disc luminosity is larger than the sphere luminosity by about an order of magnitude. This results from the steeper $q = 2$ required in the spherical case, compared to $q = 1.3$ in the disc case, to derive the same flat continuum slope, using the same N_0 in both geometries.

The second row of panels presents the dependence on q (eq.13). The values of q , noted near each curve, were selected to produce spectral slopes of $-0.5, -0.18$ and 0.45 for a disc, and $-0.5, 0$ and 0.45 for a sphere, based on the analytical expressions given in eq.56 and eq.66. The slopes derived from the numerical solutions are $-0.42, -0.11, 0.41$ for the disc, and $-0.3, 0.01, 0.45$ for the sphere, which implies that the analytic estimate is typically accurate to better than 0.1. The overall trend is that a larger q yields a flatter slope, as expected as a larger drop in the density yields a larger drop in the synchrotron emission with radius. Since the outer radius contributes at lower frequencies, a higher q implies the inner region dominates, leading to a flatter spectral slope.

If q is low enough (0.9 for a disc, 1.7 for a sphere), the emission from the outer disc becomes dominant enough, that the optically thin tail it produces at higher frequencies dominates the emission from the inner disc. The observed emission is effectively all produced by emission from a single uniform emitter at the outer disc, rather than by a superposition of emitters at all radii. The spectrum is then a steeply rising optically thick spectrum at low enough frequencies, has a peak where the outer disc becomes optically thin, and shows an optically thin tail at high frequencies, somewhat similar to the spectra observed in GHz peaked radio loud sources (O’Dea 1998; Sadler 2015).

The q values in the spherical case are steeper than in the disc case, for the same spectral slope. This is expected since the change of the synchrotron emissivity with radius depends on the change in the column density with radius. In the disc case q also provides the radial dependence of the column density, while in the sphere case the column density scales as $q + 1$.

The flat spectrum in the spherical geometry case implies $q = 2$ for both PL and thermal electrons. This implies that the gas thermal energy density $3NkT$ is a fixed fraction of the radiation energy density $L/4\pi R^2 c$. A bolometric luminosity of $L \simeq 10^{46}\text{erg s}^{-1}$ corresponds to $L_{\nu} \simeq 10^{30}\text{erg s}^{-1}\text{Hz}^{-1}$ at 10 GHz, which is produced by a corona with $NkT = 1380\text{erg cm}^{-3}$ at $R = 3R_S = 9 \times 10^{13}\text{cm}$ for the PL case (Fig.7 upper right panel). This implies a fixed energy density ratio of 4×10^{-4} at all radii.

The third row of panels in Fig.7 presents the effect of deviation from equipartition, explored by varying B/B_{eq} from 0.1 to 100, while the PL electrons remain in equipartition with the thermal plasma energy density. As expected, the luminosity in the intermediate range of frequencies increases with B/B_{eq} . In the optically thick range (low frequencies), we get the opposite effect as the luminosity decreases with increasing B/B_{eq} . That happens because the source function, $S_{\nu} = \frac{P_{\nu}}{4\pi\alpha_{\nu}}$, where P_{ν} is the emission coefficient (eq.47), and α_{ν} is the absorption coefficient (eq.28), is $\propto B^{-1/2}$. Some of the disc models lead to spectra which

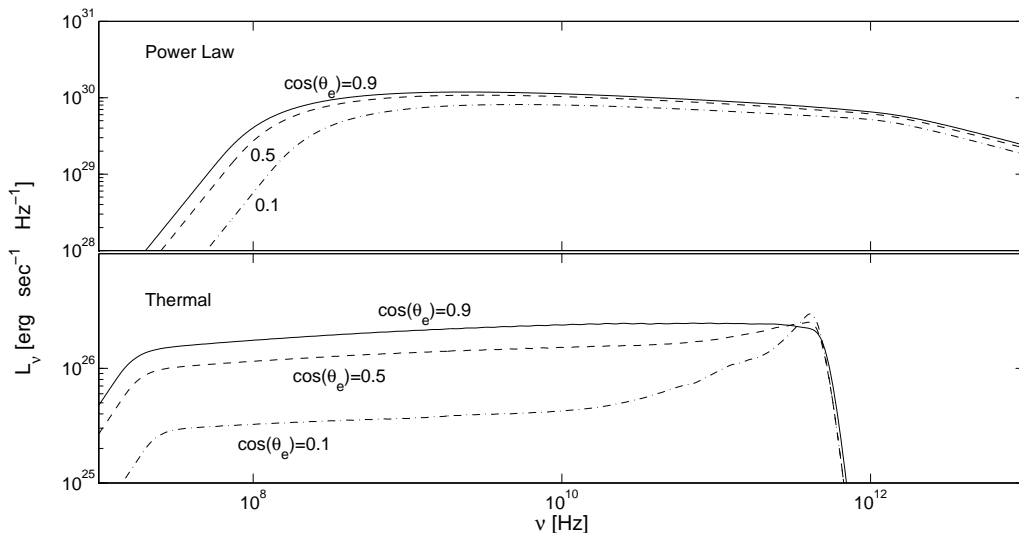


Figure 6. The inclination dependence of coronal disc emission for thermal and PL electrons. At the low frequencies the emission is optically thick, which produces a $\cos \theta_e$ dependence. At high frequencies the entire disc becomes optically thin, and the emission becomes isotropic. In the thermal case the exponential drop when the emission is optically thin leads to negligible emission, and the integrated emission is dominated by the optically thick regions. The rise in the emission for $\cos \theta_e = 0.1$ with frequency for thermal electrons is a geometry effect (see section 5)

are optically thick ($\nu^{2.5}$) at $\nu > 1$ GHz. Such optically thick synchrotron emission is not observed in RQ AGN, even on mas scales. (Barvainis et. al 2005; Kukula et al. 1998; Ulvestad et. al 2005a). Thus, according to our model, the synchrotron source needs to extend up to $R_{\max} > 3$ pc to push the spectral turnover to lower frequencies. In contrast, most spherical corona models presented here become optically thick at frequencies well below 1 GHz for the assumed $R_{\max} = 3$ pc.

Figure 8 explores the dependence of thermal synchrotron emission on various model parameters, as done in Fig.7 for the PL electrons. Here, however, we explore the dependence on N and T separately, and not just on NkT , as the synchrotron is produced by the thermal plasma, in contrast with the PL electrons where the thermal plasma is used only to set the equipartition energy density of the PL electrons. The thermal plasma luminosity is significantly weaker than the PL luminosity, for the same parameters, as found for coronally active stars (Gudel 2002; Massi & Chiuderi-Drago 1992). Another general difference from the PL emission is the sharp drop at $\nu \sim 10^{11} - 10^{13}$ Hz of the thermal synchrotron, in contrast with the transition to optically thin synchrotron with a slope of $-1/2$.

The upper panel in Fig.8 shows the sharp dependence of the thermal synchrotron luminosity on T , where L_ν increases by a factor of 725 when T increases by a factor of 5 to 5×10^9 K. This is expected since $\nu_{\text{peak}} \propto T^{1.42}$ (eq.36), while $L_\nu \propto \nu_{\text{peak}}^2 T$ (eq.41), which gives $L_\nu \propto T^{3.84}$. The numerical solution presented here yields $L_\nu \propto T^{4.09}$.

At low frequencies, where the emission is optically thick, the spectrum is independent of N , q , and B/B_{eq} , and depends only on T , as expected since the emission becomes a blackbody emission. The dependence of the emission in the

flat part of the spectrum on q , N_0 , and B/B_{eq} , is similar to the one presented by the PL electrons, as discussed above.

5.4 The dependence on the PL electrons energy slope

The value of $\delta = 2$, used above for the PL electron energy distribution, is motivated by the Fermi acceleration mechanism, and is observed in various systems. Steeper values are expected when additional electron cooling processes are taken into account (Longair 1994). The optically thin emission for $\delta = 2$ is $\nu^{-\frac{\delta-1}{2}}$. However, steeper spectra are commonly observed in RQ AGN (Kukula et al. 1998; Ulvestad et. al 2005a; Barvainis et. al 2005; Behar et al. 2015), which imply larger values of δ are present.

Figure 9 compares some of the earlier spectra with the spectra derived for the $\delta = 3$ case. As expected, the spectra are steeper, keeping the other model parameters fixed. Alternatively, higher q values are required to derive a flat spectral slopes, as can also be seen from the analytical derivation above (eq.57). A major difference is the drop in L_ν by about a factor of 100, for models with a similar spectral slope. This results from the fact that the integrated electron energy in the $\delta = 3$ case is concentrated near γ_{\min} , rather than being evenly spread between γ_{\min} and γ_{\max} per logarithmic bin in γ , which is the case for $\delta = 2$.

5.5 The effect of a larger R_{in}

The inner disc boundary assumed above is $R_{\text{in}} = 3R_S$, as expected for a viscous accretion disc around a Schwarzschild black hole. However, studies of the observed UV spectral

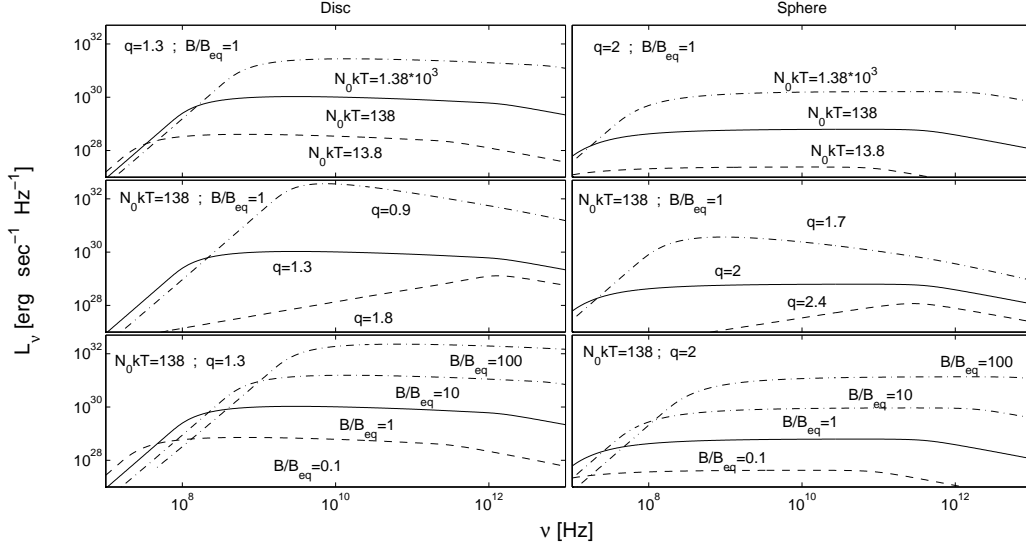


Figure 7. The spectra of PL electrons in a disc (left panels) and spherical (right panels) coronae. All calculation assume $T = 10^9 K$, $\delta = 2$, $R_0 = 3R_S$, $R_{\max} = 3 \times 10^5 R_S$, for $M_{\text{BH}} = 10^8 M_\odot$. Each panel notes the assumed values of $N_0 kT$ (in cgs at R_0), q of the density distribution, and B/B_{eq} . In all cases, the disc luminosity is higher than the sphere luminosity, for similar parameters. The upper panels present the dependence on the equipartition energy density, as noted by the value of $N_0 kT$. The emission remains optically thick (slope of 2.5) to higher frequencies, with increasing $N_0 kT$, leading to higher luminosities in the flat part of the spectrum. The middle panels present the q values required to derive slopes of about 1/2, 0, and $-1/2$ in the flat part of the spectrum. In all cases the q values of the spherical case are steeper than the disc case. The lower panels present the effect of the deviations of B from equipartition. The luminosity in the optically thick part decreases with increasing B , and rises with B in the flat slope region. Note that some of the models lead to optically thick emission at $\nu > 1\text{GHz}$, which is not observed.

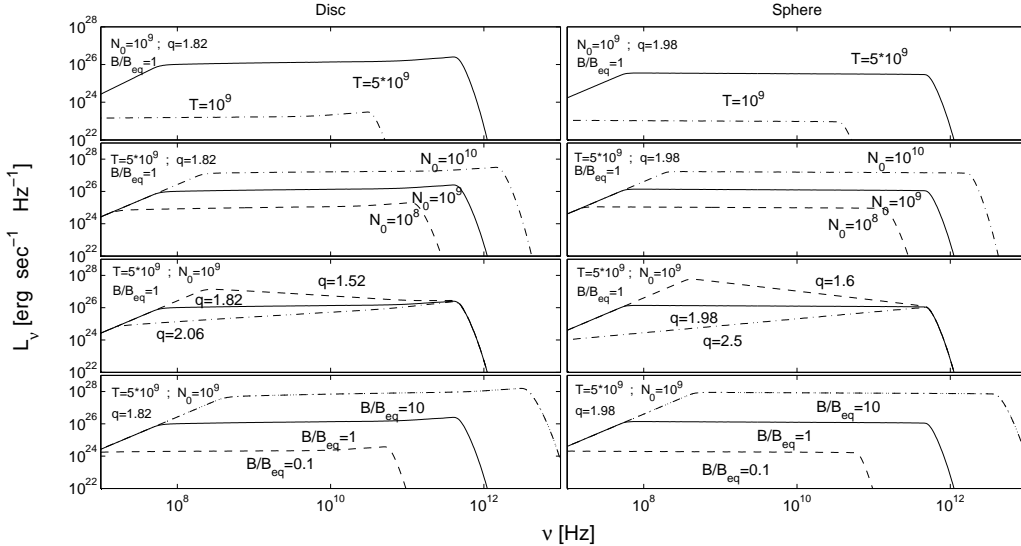


Figure 8. The spectra of thermal electrons confined within a disc (left panels) and spherical (right panels) coronae. The other model parameters are the same as for the PL electrons (see caption of Fig.7). The upper panel show the sharp dependence of the luminosity on T , as expected since analytic considerations give $L_\nu \propto T^{3.84}$ (see text). Note the overlap of the models in all panels, at the same T , in the optically thick part, where the emission becomes a blackbody. Note also the sharp spectral break at high energies, when the whole configuration becomes optically thin, in contrast with the $-1/2$ slope of the optically thin PL emission. The emission in the flat part of the continuum shows similar dependence on the parameters explored, to the one shown by the PL electrons (Fig.7).

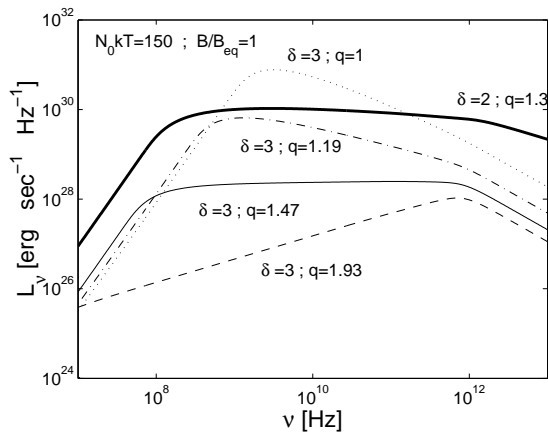


Figure 9. A comparison of the spectra of disc coroneae for electron PL distributions with $\delta = 2$ and $\delta = 3$. As expected, the spectra in the $\delta = 3$ case are steeper. The q values required to derive spectral slopes of approximately -1 , $-1/2$, 0 and $1/2$ are marked near each curve. Note the factor ~ 100 drop in the flat L_ν for the $\delta = 3$ case, compared to the $\delta = 2$ case (see text).

energy distribution of AGN, together with theoretical arguments, suggest the thin disc solution may break at a few 10 s of R_S (Laor & Davis, 2014), below which the accretion flow may change its nature (e.g. become a low radiative efficiency geometrically thick flow). If the corona is formed only above the surface of a thin disc, it may not extend down to $3R_S$. For the specific model parameters used here, $M_{BH} = 10^8 M_\odot$ shining at the Eddington luminosity, we get that $R_{in} = 17R_S$ from the analytic solution in Laor & Davis, (2014).

Figure 10 shows the effect of increasing R_{in} on the observed spectrum from a disc corona of PL electrons. For the sake of completeness, the figure also shows the effect of a larger R_{in} for a spherical corona. As expected, the frequency of the spectral break from a flat slope to an optically thin slope, decreases with increasing R_{in} , from ~ 1 THz to a few hundred GHz, as the highest emission frequency originates from the smallest radii (see Fig.10). One can also estimate the change in the break frequency by applying the analytic estimate for ν_{peak} for the innermost disc parameters. One can use this break frequency to deduce the properties of the innermost corona. However, the spectral range above ~ 300 GHz is likely dominated by the Rayleigh-Jeans tail of the coldest dust emission (Hughes et al. 1993; Haas et al. 2000, 2003), which rises extremely steeply and heavily dominates the emission above ~ 300 GHz. The dust emission may be overcome by VLBI observations, which exclude sources with $T_b < 10^8$ K, and may be able to overcome the strong background dust emission, and detect the expected synchrotron turnover in the emission of a compact mas size source at the centre.

6 DISCUSSION

The PL X-ray emission in AGN indicates the presence of coronal gas close to the centre. Since coronal emission in stars is associated with synchrotron radio emission, this raises the possibility that the radio emission in RQ AGN is also of coronal origin, in particular since RQ AGN fol-

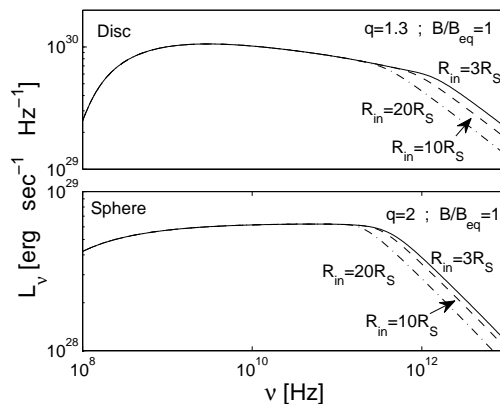


Figure 10. The effect of increased R_{in} on the observed spectral shape from a PL electron distribution. The values of R_{in} are noted near each curve for the disc and sphere geometries. As expected, the break frequency from a flat PL emission, to the steeper optically thin emission, decreases with increasing R_{in} . The spectral range at $\nu > 3 \times 10^{11}$ Hz is heavily dominated by dust emission, but it should be excluded by VLBI observations, which measure only the $T_b > 10^8$ K component. This spectral turnover can be used to probe the coronal R_{in} .

low the radio versus X-ray luminosity relation displayed by stellar coronal emission (Gudel & Benz 1993; LB08). The synchrotron emission can be produced by the coronal hot thermal electrons, which also produce the X-ray emission. Or, it may be produced by PL electrons within the coronal gas. These PL electrons may be produced by magnetic activity in the corona, specifically magnetic reconnection events, as seen in stellar coronae. The radio synchrotron emission then serves as an indicator for the coronal heating, while the X-rays give the total coronal cooling (free-free in stellar coronae, and Comptonization in AGN coronae), leading to the observed relation between the two. The PL electrons can also be produced by shock acceleration, rather than reconnection, and may still serve as an indicator for the coronal heating, if it is due to shocks. Alternatively, the radio and X-ray relation may result from the fact that both are produced by the same thermal electrons, which reside in a medium with a given ratio of magnetic to radiation energy density.

Here we provide analytic estimates for the spectral slope and luminosity produced by thermal and PL electrons, embedded in a magnetic field in either a disc or a spherical configuration. We present numerical solutions, and explore the solution parameter space, which can produce the observed $L_\nu \sim 10^{28} - 10^{30} \text{ erg s}^{-1} \text{ Hz}^{-1}$ at $\nu \sim 1 - 100$ GHz, which characterizes RQ AGN at a bolometric luminosity of $10^{44} - 10^{46} \text{ erg s}^{-1}$ (e.g. LB08). We concentrate here on models which yield flat spectra, as this is the signatures of compact radio sources, such as AGN coronae.

Based on the typical rapid X-ray variability, the X-ray corona must be compact. In contrast, the GHz radio corona must be on a pc scale. The models explored here allow to relate the GHz emission to the emission at few hundred GHz, which is expected to originate from the X-ray corona. As discussed in paper II, the much larger radio corona does not produce significant X-ray emission, given the weakness

of the disc flux on large scales, which is the source for the Compton cooling X-ray emission of the corona.

6.1 Comparison with observations

Do the observed spectral slope in the radio indeed indicate significant emission from a compact source? Are the spectra steep, indicating an optically thin synchrotron source with a size of a pc or larger, or are the spectra flat, indicating the dominance of a compact optically thick source? Barvainis et al. (1996) find in 39 RQ AGN that the spectral shapes cover a wide range, with 40% of the objects showing a flat or even rising spectral slopes. Similar results are obtained in follow-up studies. Kukula et al. (1998) find that 46% (11/24) of RQ AGN have $\eta > -0.2$, and 54% $\eta < -0.6$, at 4.8-8.4 GHz, and Barvainis et al. (2005) find 45% (5/11) have $\eta > 0.19$ and 55% $\eta < -0.52$, also at the same frequency range. Interestingly, with the small statistics available, the spectral slope distribution appears to cluster at either steep or flat slopes, for both type 1 and type 2 AGN (Ulvestad & Ho 2001; Lal & Ho 2010). This suggests that the more extended optically thin source, and the compact optically thick source do not go together, they are either unrelated, or anti correlated.

As noted above, significant unresolved pc scale radio emission is also derived from VLBI observations (Blundell & Beasley 1998; Caccianiga et al. 2001; Middelberg et al. 2004; Ulvestad et al. 2005a; Ulvestad et al. 2005b; Giroletti & Panessa 2009; Doi et al. 2013; Panessa & Giroletti 2013). In the case of NGC 1068, the pc scale emission is spatially resolved as coming from a disc structure, but significant emission arises from structures on larger scales (Gallimore et al. 1997, 2004). The spectrum of the pc scale emission is generally flat, while the extended emission is steep, which indicates the high frequency emission is likely dominated by the compact emission source.

As noted by Barvainis et al. (1996; 2005), a significant fraction of the flat spectra sources show variability, while none of the steep spectra sources varies on a timescale of months. A result consistent with the synchrotron emission models, where the flat sources need to be compact. The size of the 5 GHz emitting region is similar to the size of the Broad Line Region, of $0.1L_{46}^{1/2}$ pc, where $L_{46} = L_{\text{bol}}/10^{46} \text{ erg s}^{-1}$ (LB08, eq.22), allowing significant variability on the observed months timescale.

Observations therefore clearly indicate that the coronal models, which predict a compact emission region, may be valid in a significant fraction of AGN. The more extended emission may also be powered by magnetized plasma ejected from the central compact source, however such an extended component is not considered here.

6.2 Comparison with earlier models

A common interpretation for the radio emission in RQ AGN is a scaled down jet, compared to the jet in RL AGN (Falcke et al. 1995). Apart from one possible exception (Blundell et al. 2003), VLBI monitoring of nearby RQ AGN detect either a static or slowly moving radio sources (Ulvestad et al. 2005a; Reynolds et al. 2009), which argues

against relativistic jets. A weak, non relativistic, small scale jet is basically a cloud of magnetized plasma, and differs from a corona only in terms of the geometry. Since the physical size may be pc or smaller for both coronae and weak jets, it may remain unresolved, and therefore VLBI imaging may not be able to differentiate the two.

Since there are no robust prediction for the physical properties of a magnetized plasma in a weak jet, versus a corona, one cannot currently differentiate the two models just based on the predicted synchrotron emission.

As mentioned earlier, radio emission may also be produced by the interaction of an AGN driven wind with the host galaxy interstellar medium. The radio emitting shock fronts are expected to be on tens to a hundred pc scales (Jiang et al. 2010), and possibly out to kpc scale (Nims et al. 2015). In contrast, the spherical coronal models explored here are much more compact, and produce the observed luminosity on a scale of a single pc. Spatially, the wind interaction region may be resolved on VLBI mas scale imaging, which should show emission from the shock front surface. In contrast, a magnetized CME may produce synchrotron from the whole volume. However, the later case will be resolved only in nearby AGN (closer than 200 Mpc, for a 1 mas resolution).

A major difference, which results from the different physical sizes, is the spectral slope. The size in the wind scenario suggests that the synchrotron emission will be optically thick only at frequencies well below a GHz (LB08), and will therefore be optically thin with $\eta \leq -0.5$ at 1-100 GHz (unless the emission is highly clumped). In the CME case, $\eta > -0.5$ is possible, where the exact value depends on the radial density and temperature distributions (see eqs.63, 66). As noted above, about half of the RQ AGN are characterized by $\eta > -0.3$, which argues strongly against the wind scenario in these objects.

If the wind scenarios apply, the observed radio emission should not vary on timescales of a few years or shorter, while the compact coronal models allow variability on timescales of a year and faster. As noted above, the observations suggest significant variability on timescales of months and below in some of the RQ AGN, which clearly rules out the wind scenario as the dominant mechanism in these objects.

Furthermore, if the spectral slope is flat, then the observed emission is a superposition of optically thick sources with a range of sizes, and the variability timescale is expected to decrease with increasing frequency, as possibly observed in NGC 7469 (Baldi et al. 2015).

6.3 Thermal Synchrotron

Is the thermal synchrotron a viable solution? Here we find that the thermal synchrotron from an isothermal corona with $T \simeq 5 \times 10^9$ K, as suggested by recent hard X-ray observations (Fabian et al. 2015), is a factor of $\sim 10^4$ lower than the emission of PL electrons, for similar model parameters (see Fig.8). Thermal synchrotron can reach the observed luminosities assuming a higher temperatures. Since the thermal synchrotron follows $L_{\nu_{\text{peak}}} \propto T^{4.09}$ (section 5.3), a value of $T \simeq 5 \times 10^{10}$ K is required for the thermal synchrotron to reach the synchrotron emissivity. This result can be understood analytically by comparing the synchrotron source

function $S_\nu = 2.9 \times 10^{-31} B^{-1/2} \nu^{5/2} \text{ erg cm}^{-2} \text{ Hz}^{-1} \text{ Strd}^{-1}$ (eq.17 in LB08 for $\delta = 2$), to the blackbody source function $B_\nu = 3.1 \times 10^{-37} \nu^2 T \text{ erg cm}^{-2} \text{ Hz}^{-1} \text{ Strd}^{-1}$ in the Rayleigh-Jeans limit. This implies one needs $T \sim 10^6 \nu^{1/2} B^{-1/2} \text{ K}$, or $T \sim 10^{11} \text{ K}$ (for $\nu = 10^{10} \text{ Hz}$, $B = 1 \text{ Gauss}$) for the thermal synchrotron to become comparable to the synchrotron emission. The required T can also be estimated by equating the energy of the electrons emitting at a given frequency, $\nu = 4.1\gamma^2 B \text{ MHz}$, to kT . Such a high value for T appears to be excluded by X-ray observations (though these apply to the X-ray corona, rather than the much larger radio corona at a few GHz). Such a high temperature is not expected from magnetic reconnection, and may also be excluded by pair production arguments, as discussed above (section 1).

Alternatively, thermal synchrotron from a $T \simeq 5 \times 10^9 \text{ K}$ corona may still be viable, if the emitting surface is significantly larger. As noted above, current VLBI observations lead to minimal brightness temperatures $\sim 10^9 \text{ K}$, and therefore do not exclude such thermal synchrotron.

The signature of thermal synchrotron is an exponential cutoff in the emission above a few hundred GHz, where the most compact emitting region becomes optically thin (eq.36). This results from the exponential cutoff in the maximal electron energy density in the relativistic Maxwell Boltzmann distribution (eq.14). This is in contrast with the PL distribution, where the a maximal $\gamma = 3000$ assumed here, ensures the peak emission is beyond 1000 GHz (section 3). If there is a break in the PL electron energy distribution, it will also be associated by a corresponding spectral break at $\nu = 4.1\gamma^2 B \text{ MHz}$ (in the optically thin case). However, the break will be to a steeper PL emission, rather than the sharp exponential break of the thermal synchrotron.

6.4 Coronal properties

Is a thin corona at $T \simeq 5 \times 10^9 \text{ K}$, which extends out to say $3 \times 10^5 R_S$, (3 pc in our model) a viable solution? This temperature is likely well above the escape speed from the disc surface at such a large radius. Therefore, the corona needs to be magnetically confined to avoid a thermal wind with a considerable mass loss. The assumed equipartition magnetic field strength is consistent with the value required by the magnetic confinement assumption.

Since the system is powered by accretion, can accretion provide enough energy to power the radio emission? The fraction of the rest mass energy dissipated in accretion from infinity to R is $\epsilon = R_S/R$ in the Newtonian limit (and a factor 3 larger in viscous accretion disc). At the outer radius therefore $\epsilon \sim 10^{-5}$. Since the bolometric luminosity L_{bol} is likely derived from $\epsilon \sim 0.1$, we expect that accretion can provide $L_{\text{radio}}/L_{\text{bol}} \sim 10^{-4}$, which is well above the observed relation of $L_{\text{radio}}/L_{\text{bol}} \sim 10^{-6}$ (using $L_{\text{radio}}/L_{\text{X-ray}} \sim 10^{-5}$, and $L_{\text{X-ray}}/L_{\text{bol}} \sim 0.1$).

Clearly, the disc at such a large radius is self-gravitating and rather cold. Whether it can indeed maintain a thin magnetically confined hot corona at its surface is an open question.

Alternatively, and maybe more plausibly, the corona is in a spherical configuration. Although the solution here is assumed static, such a configuration is likely formed by an outflow, i.e. a CME produced by coronal activity in the inner disc. In this case there is no need to confine the coronal

gas, and its power may come from the energy embedded in it when it is ejected. Interestingly, a flat spectral slope is obtained for $q = 2$, as expected in a uniform velocity outflow (the likely wind solution at large radius). The coronal energy density required to get the observed $L_\nu \sim 10^{30} \text{ erg s}^{-1} \text{ Hz}^{-1}$ is $u_{\text{corona}} \sim 1400 \text{ erg cm}^{-3}$ (Fig.7, upper right panel) at R_0 . Since it scales at R^{-2} , the ratio to the radiation energy density of the AGN $u_{\text{radiation}} = L_{\text{bol}}/4\pi R^2 c$ remains constant. For $L_{\text{bol}} = 10^{46} \text{ erg s}^{-1}$, which corresponds to the above L_ν at $\nu \sim 10 \text{ GHz}$, one gets $u_{\text{corona}}/u_{\text{radiation}} = 4 \times 10^{-4}$. The corona is therefore a dynamically negligible component. This constant ratio is interesting, and may provide some hints for the coronal heating mechanism.

7 CONCLUSIONS

We explore the possible radio emission from either a flat or a spherical magnetized corona, powered by either PL or thermal electrons. We concentrate on flat spectra models, which characterize about half of RQ AGN, and is the main signature of a compact emission region such as a corona. Our main conclusions are as follows:

1. A flat spectral slope in the 1-1000 GHz range requires the superposition of synchrotron emission from the innermost region at $3R_S$ to $3 \times 10^5 R_S$ ($3 \times 10^{-5} \text{ pc}$ to 3 pc). The radio corona at 1 GHz emission comes from the largest scales, and should be resolved in mas resolution VLBI observations of nearby AGN (closer than $\sim 100 \text{ Mpc}$). The few 100 GHz emission corona overlaps in size the X-ray corona, and its size can only be constrained from its variability timescale.

2. The synchrotron emission at a given frequency, is produced over a wide range of radii for PL electrons. In contrast, the synchrotron emission of thermal electrons at a given frequency, originates from a narrow range of radii.

3. The synchrotron emission from a disc corona of PL electrons is nearly isotropic, as most of the emission originates from the optically thin outer regions. The emission of thermal electrons from a disc corona shows a $\cos(\theta)$ dependence, as the observed emission is dominated by the outermost optically thick region.

4. A luminosity of $L_\nu \sim 10^{30} \text{ erg s}^{-1} \text{ Hz}^{-1}$ can be produced by PL electrons, magnetic field, and a corona, which are all in equipartition, with an energy density which scales roughly as R^{-1} , and $NkT \sim 1000 \text{ erg cm}^{-3}$ at $3R_S$. In the spherical corona configuration, the energy density scales as R^{-2} . For PL electrons synchrotron, this equipartition energy density is a constant fraction of $\sim 4 \times 10^{-4}$ of the central source radiation density.

5. Thermal synchrotron from $T \simeq 5 \times 10^9 \text{ K}$ electrons, as suggested by recent hard X-ray observations, under predicts the radio L_ν by a factor of $\sim 10^4$. To be a valid mechanism the emitting surface must be significantly larger than assumed here, but it is not yet in contradiction with current VLBI observations. Alternatively, one needs $T \simeq 5 \times 10^{10} \text{ K}$ to derive the observed luminosity at $\nu \sim 10 \text{ GHz}$.

6. At $\nu = 300\text{-}1000 \text{ GHz}$ the innermost corona is expected to become optically thin, and the spectrum is expected to show a spectral break. The position of this break can be used to probe the innermost coronal size. It should display a sharp cutoff, rather than a steeper PL, in case of thermal synchrotron emission. Since dust heavily dominates

this spectral range, the detection requires VLBI observations, which exclude the low T_b dust emission.

Additional constraints on the radio and X-ray coronal properties can be derived by including the observed X-ray emission, in particular the enigmatic Gudel-Benz relation of $L_R/L_X \sim 10^{-5}$, which is explored in paper II

Clearly, further exploration of the radio emission in RQ AGN, in particular at the mm range (Behar et al. 2015), will allow to probe directly the distribution of relativistic electrons and magnetic fields closest to the centre. The relation of the mm emission with the X-ray emission, in particular their variabilities (Baldi et al. 2015), can provide important insights for the physical mechanisms which power accretion disc coronae in RQ AGN.

ACKNOWLEDGEMENTS

We thank the referee, Nadia Zakamska, for the exceptionally thorough and helpful review. We also thank R. Sunyaev for suggesting to explore the coronal thermal synchrotron emission. This research was supported by the Israel Science Foundation (grant no. 1561/13).

REFERENCES

- Anderson, J. M., & Ulvestad, J. S. 2005, ApJ, 627, 674
 Baldi, R. D., Behar, E., Laor, A., & Horesh, A. 2015, MNRAS, 454, 4277
 Barvainis, R., Lonsdale, C., & Antonucci, R. 1996, AJ, 111, 1431
 Barvainis R., Lehar J., Birkinshaw M., Falcke H., Blundell K.M., 2005, ApJ, 618, 108
 Behar, E., Baldi, R. D., Laor, A., et al. 2015, MNRAS, 451, 517
 Blundell, K. M., & Beasley, A. J. 1998, MNRAS, 299, 165
 Blundell, K. M., Beasley, A. J., & Bicknell, G. V. 2003, ApJ, 591, L103
 Caccianiga, A., Marchā, M. J. M., Thean, A., Dennett-Thorpe, J. 2001, MNRAS, 328, 867
 Condon, J. J., Kellermann, K. I., Kimball, A. E., Ivezić, Ž., & Perley, R. A. 2013, ApJ, 768, 37
 Di Matteo, T., Blackman, E. G., & Fabian, A. C. 1997, MNRAS, 291, L23
 Di Matteo T., 1998, MNRAS, 299, L15
 Doi, A., Asada, K., Fujisawa, K., et al. 2013, ApJ, 765, 69
 Fabian, A. C., Lohfink, A., Kara, E., et al. 2015, MNRAS, 451, 4375
 Falcke, H., Malkan, M. A., & Biermann, P. L. 1995, A&A, 298, 375
 Gallimore, J. F., Baum, S. A., & O’Dea, C. P. 1997, Nature, 388, 852
 Gallimore, J. F., Baum, S. A., & O’Dea, C. P. 2004, ApJ, 613, 794
 Gallimore, J. F., Axon, D. J., O’Dea, C. P., Baum, S. A., & Pedlar, A. 2006, AJ, 132, 546
 Giroletti, M., & Panessa, F. 2009, ApJL, 706, L260
 Gudel M., 2002, ARA&A, 40, 217
 Gudel M., Benz A.O., 1993, ApJ, 405, L63
 Haardt F, Maraschi L., 1991, ApJ, 380, L51
 Haardt F, Maraschi L., 1993, ApJ, 413, 507
 Haas, M., Müller, S. A. H., Chini, R., et al. 2000, A&A, 354, 453
 Haas, M., Klaas, U., Müller, S. A. H., et al. 2003, A&A, 402, 87
 Hughes, D. H., Robson, E. I., Dunlop, J. S., & Gear, W. K. 1993, MNRAS, 263, 607
 Inoue, Y., & Doi, A. 2014, PASJ, 66, L8
 Ishibashi, W., & Courvoisier, T. J.-L. 2011, A&A, 525, A118
 Jiang Y.F., Ciotti L., Ostriker J.P., Spitkovsky A., 2010, ApJ, 711, 125
 Kellermann K.I., Sramek R., Schmidt M., Shaffer D.B., Green R., 1989, AJ, 98, 1195
 Kellermann K.I., Sramek R., Schmidt M., Shaffer D.B., Green R., 1994, AJ, 108, 1163
 Kukula M.J., Dunlop J.S., Hughes D.H., Rawlings S., 1998, MNRAS, 297, 366
 Lal, D. V., & Ho, L. C. 2010, AJ, 139, 1089
 Laor A., Behar E., 2008, MNRAS, 390, 847 (LB08)
 Laor A., Davis S. W., 2014, MNRAS, 438, 3024
 Leipski, C., Falcke, H., Bennert, N., Huettemeister, S. 2006, A&A, 455, 161
 Lightman, A. P., & Zdziarski, A. A. 1987, ApJ, 319, 643
 Longair, M. S. 1994, High energy astrophysics. Volume 2. Stars, the Galaxy and the interstellar medium., by Longair, M. S.. Cambridge University Press, Cambridge (UK), 1994, 410 p., ISBN 0-521-43439-4
 Mahadevan R., Narayan R., Yi I., 1996, ApJ, 465, 327
 Massi M., Chiuderi-Drago F., 1992, A&A, 253, 403
 Merloni, A., & Fabian, A. C. 2002, MNRAS, 332, 165
 Middelberg, E., Roy, A. L., Nagar, N. M., et al. 2004, A&A, 417, 925
 Miller, P., Rawlings, S., & Saunders, R. 1993, MNRAS, 263, 425
 Mundell, C. G., Ferruit, P., Nagar, N., & Wilson, A. S. 2009, ApJ, 703, 802
 Nims J., Quataert E., Faucher-Giguère C., 2015, MNRAS, 447, 3612
 O’Dea, C. P. 1998, PASP, 110, 493
 Padovani, P., Miller, N., Kellermann, K. I., et al. 2011, ApJ, 740, 20
 Panessa, F., & Giroletti, M. 2013, MNRAS, 432, 1138
 Reynolds, C., Punsly, B., Kharb, P., O’Dea, C. P., & Wrobel, J. 2009, ApJ, 706, 851
 Rybicki G.B, Lightman A.P., 2004, Radiative Processes in Astrophysics, Second edition. WILEY-VCH Verlag GmbH & Co. KGaA, Weinheim, Germany, (RL04)
 Sadler, E. M. 2015, arXiv:1512.01851
 Shakura N.I, Sunyaev R.A., 1973, A&A, 24, 337
 Svensson, R. 1984, MNRAS, 209, 175
 Ulvestad, J. S., & Ho, L. C. 2001, ApJ, 558, 561
 Ulvestad J.S., Antonucci R.R.J., Barvainis R., 2005a, ApJ, 621, 123
 Ulvestad, J. S., Wong, D. S., Taylor, G. B., Gallimore, J. F., & Mundell, C. G. 2005b, AJ, 130, 936
 Wardzinski G., Zdziarski A.A., 2000, MNRAS, 314, 183
 White, S. V., Jarvis, M. J., Häußler, B., & Maddox, N. 2015, MNRAS, 448, 2665
 Wilson, A. S., & Colbert, E. J. M. 1995, ApJ, 438, 62
 Wrobel, J. M. 2000, ApJ, 531, 716
 Zakamska, N. L., & Greene, J. E. 2014, MNRAS, 442, 784
 Zakamska, N. L., Lampayan, K., Petric, A., et al. 2016,

MNRAS, 455, 4191

Zheleznyakov V.V, 1970, Radio Emission of the Sun and Planets. Pergamon Press , Oxford , UK

Zuther, J., Fischer, S., & Eckart, A. 2012, A&A, 543, A57